

www.acsanm.org Article

# Synergistic Effect of $TiS_3$ and $Ti_3C_2T_x$ MXene for Temperature-Tunable p-/n-Type Gas Sensing

Michael J. Loes, Saman Bagheri, Nataliia S. Vorobeva, Jehad Abourahma, and Alexander Sinitskii\*



Cite This: ACS Appl. Nano Mater. 2023, 6, 9226–9235



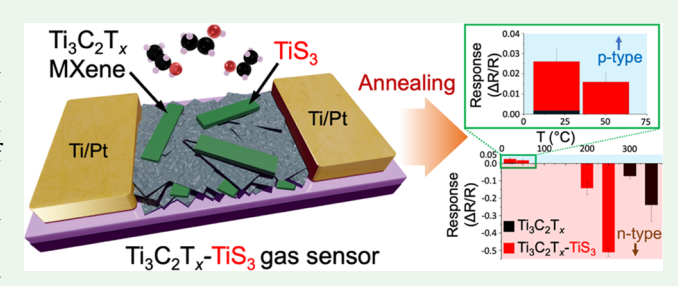
**ACCESS** I

III Metrics & More

Article Recommendations

Supporting Information

**ABSTRACT:** We propose a strategy for highly tunable gas sensors, in which a MXene is combined with a sacrificial material that could be controllably oxidized upon mild annealing to form oxide nanoparticles that alter the sensing response. A controlled annealing of such composite generally retains the integrity of MXene sheets while gradually converting the sacrificial material to a metal oxide that could form semiconductor heterojunctions with MXene, fine-tuning its sensor properties. This strategy is demonstrated using gas sensors based on Ti<sub>3</sub>C<sub>2</sub>T<sub>x</sub> MXene mixed with TiS<sub>3</sub>, a semiconducting transition metal trichalcogenide.



Compared to pristine MXene, the  $Ti_3C_2T_x$ - $TiS_3$  composite exhibited a significantly improved sensor response to ethanol, which served as a model analyte, both at room temperature and upon annealing. Furthermore, as a less thermally stable material than the MXene,  $TiS_3$  oxidizes faster than  $Ti_3C_2T_x$  at elevated temperatures, producing  $TiO_2$  nanoparticles that strongly affect the sensing response. A pristine  $Ti_3C_2T_x$  exhibits a p-type sensor response to ethanol at room temperature. Upon annealing,  $Ti_3C_2T_x$  gradually degrades to  $TiO_2$ , changing the sensor response to n-type above  $\sim 300$  °C. The addition of  $TiS_3$  allows for the general preservation of MXene as the sensor material, as the temperature of the p-n transition decreases to about 200 °C, at which  $Ti_3C_2T_x$  is generally stable. This approach can likely be applied to a great variety of combinations of various MXenes and sacrificial compounds with sensor properties that could be tuned *via* annealing for specific analytes or applications.

**KEYWORDS:** 2D materials, MXene, titanium carbide,  $Ti_3C_2T_{xy}$   $TiS_{3y}$  gas sensors

## INTRODUCTION

MXenes are two-dimensional (2D) transition metal carbides, nitrides, and carbonitrides which are synthesized by the chemical etching of the A-layer elements from ceramic MAX phases. The general formula of MXenes is  $M_{n+1}X_nT_x$  (n=1,2,3 or 4), where M is a transition metal, X is C and/or N, and  $T_x$  represents the surface termination of MXene sheets that typically includes fluorine, oxygen, and hydroxyl groups. MXenes have recently attracted the attention of the gas sensing community owing to their exceptional chemical diversity, solution processability, and high surface-to-volume ratio with the additional benefits of high electrical conductivity and the promise of tunable surface chemistry.  $^{4-8}$ 

 ${
m Ti}_3{
m C}_2{
m T}_x$  is the most well-studied member of the MXene family to date<sup>1</sup> and has been shown to be sensitive toward many volatile compounds, such as acetone, various low-molecular-weight alcohols, and ammonia,<sup>9–11</sup> with low electronic noise<sup>9</sup> and the possibility of room-temperature sensing. Many device architectures have been explored, but a simple drop-cast film of MXene bridging two or several electrodes remains the most approachable and the most popular 4,9–13 owing to the high solubility of MXenes in many solvents. It is important to note that  ${
m Ti}_3{
m C}_2{
m T}_x$  was reported to have metallic conductivity while strong chemiresistive

response is often associated with semiconducting materials, such as metal oxides. 16,17 It is therefore not surprising that recent experiments have improved the sensing response of MXene films by decoration with TiO<sub>2</sub> nanoparticles either by co-deposition of the particles with the film 18,19 or by in situ formation of TiO2 nanoparticles by partial oxidation of the  $Ti_3C_2T_r$  sensing film. <sup>10,20-22</sup> This treatment results in the formation of heterojunctions between semiconducting TiO2 nanoparticles and metallic Ti<sub>3</sub>C<sub>2</sub>T<sub>x</sub> that create a depletion region that is more sensitive to local changes in electron density. 12,20 Noteworthy, by the latter method, homogeneous films of Ti<sub>3</sub>C<sub>2</sub>T<sub>x</sub> are subjected to oxidative treatments, resulting in the sacrifice of MXene to form TiO<sub>2</sub>. 10 Numerous reports have emerged in recent years exploring the effect of compositing semiconductor materials with MXenes<sup>12,13,23–25</sup> as well as a number of studies of the effects of oxidizing  $Ti_3C_2T_x$  MXene to  $TiO_2$  in situ. <sup>10,26,27</sup> The general consensus

Received: February 20, 2023 Accepted: May 3, 2023 Published: May 30, 2023





is that creating hybrid films with MXenes is an effective strategy for the improvement of many device characteristics including response time, sensitivity, and stability.

In this paper, we demonstrate that a mixture of  $Ti_3C_2T_x$  with a semiconducting TiS3 is a highly tunable sensing platform with improved characteristics compared to a pristine MXene. First of all, since the improved sensor performance in the previously reported examples 10,12,18,20,21 was based on nanohybrid junctions between Ti<sub>3</sub>C<sub>2</sub>T<sub>x</sub> and TiO<sub>2</sub>, the source of TiO<sub>2</sub> in the system is not important. In this work, we propose that the addition of TiS3, which is less thermally stable than Ti<sub>3</sub>C<sub>2</sub>T<sub>x</sub>, allows for the formation of TiO<sub>2</sub> particles from TiS<sub>3</sub> via annealing at temperatures sufficiently low to preserve the conductive MXene material. Because of the possibility of gradual conversion of TiS<sub>3</sub> to TiO<sub>2</sub>, the resulting Ti<sub>3</sub>C<sub>2</sub>T<sub>x</sub>-TiS<sub>3</sub> sensors exhibit a high degree of chemical tunability, which would not be achieved if TiO<sub>2</sub> was directly added to a MXene. The as-prepared Ti<sub>3</sub>C<sub>2</sub>T<sub>x</sub>-TiS<sub>3</sub> sensors exhibit a p-type response to ethanol, which was used as a model analyte, but upon annealing, the devices gradually convert to n-type sensors with progressive oxidation of TiS<sub>3</sub> to TiO<sub>2</sub>. While annealing of pristine Ti<sub>3</sub>C<sub>2</sub>T<sub>x</sub> devices resulted in qualitatively similar changes in sensor properties, 10 the Ti<sub>3</sub>C<sub>2</sub>T<sub>x</sub>-TiS<sub>3</sub> sensors outperformed them across the entire temperature range, exhibiting higher responses to the analyte and lowering the temperature necessary for the transition to the n-type behavior by about 100 °C.

Overall, the results of this work suggest a general strategy, whereby a tunable gas sensing platform is produced by mixing a MXene with a temperature-sensitive sacrificial material. Controlled annealing of such a composite retains the general integrity of MXene sheets while gradually converting the sacrificial material to a metal oxide that could form functional heterojunctions with a MXene, fine-tuning the sensor properties for a specific analyte or application.

# ■ RESULTS AND DISCUSSION

The gas sensors that were tested in this study are schematically illustrated in Figure 1a. They comprise two different nanomaterials,  ${\rm Ti_3C_2T_x}$  MXene and  ${\rm TiS_3}$ . Figure 1a (top left) shows the structure of  ${\rm Ti_3C_2T_x}$  MXene. The material is synthesized in the form of 2D flakes that contain close-packed layers of titanium atoms with carbon atoms occupying the octahedral voids. The  ${\rm Ti_3C_2T_x}$  flakes that are produced by the acid etching of  ${\rm Ti_3AlC_2}$  MAX phase<sup>28</sup> are known to be soluble in water and polar organic solvents because of their surface termination ( ${\rm T_x}$ ) with various functional groups.<sup>2,3</sup>

TiS<sub>3</sub> crystals have a very different morphology compared to Ti<sub>3</sub>C<sub>2</sub>T<sub>x</sub>. Instead of 2D flakes that are typical for MXenes, TiS<sub>3</sub> grows in the form of needle-like crystals.<sup>29-31</sup> The highly anisotropic shape of these crystals originates from the crystal structure of TiS3, which is formed by one-dimensional (1D) chains of trigonal prisms formed by sulfide (S<sup>2-</sup>) and disulfide (S<sub>2</sub><sup>2-</sup>) species connecting Ti<sup>4+</sup> centers. These 1D chains, which are oriented along the crystallographic b direction of the monoclinic TiS<sub>3</sub> structure  $(P2_1/m \text{ space group})$ , are shown in the top right inset in Figure 1a. Because of the weak interactions between these 1D chains, TiS<sub>3</sub> crystals typically exfoliate in the form of high-aspect-ratio nanoribbons with their long axes corresponding to the crystallographic b direction of TiS<sub>3</sub>.<sup>29</sup> Overall, TiS<sub>3</sub> could be a promising material for gas sensor applications because of its semiconductor properties<sup>32</sup> with a bandgap of ~1 eV,<sup>33</sup> very high



**Figure 1.**  $Ti_3C_2T_x$ - $TiS_3$  gas sensors. (a) Schemes of the structures of  $Ti_3C_2T_x$  and  $TiS_3$ , as well as the  $Ti_3C_2T_x$ - $TiS_3$  gas sensor. In the scheme of  $Ti_3C_2T_x$ , the surface functionalities  $(T_x)$  are shown as OH groups, although other moieties, such as oxygen and fluorine, can decorate MXene flakes as well.  $^{2,3}$  (b) Scanning electron microscopy (SEM) images of  $Ti_3C_2T_x$  flakes on  $Si/SiO_2$  substrate (left), as-grown needle-like  $TiS_3$  crystals (middle), and a film containing 75 wt %  $Ti_3C_2T_x$  and 25 wt %  $TiS_3$  (right).

theoretically predicted mobility,  $^{34,35}$  highly anisotropic electronic and optoelectronic properties,  $^{36-39}$  and intriguing low-temperature physics.  $^{40-44}$  Several recent studies investigated solution exfoliation of TiS $_3$  and its applications in photodetectors,  $^{45}$  printed electronics,  $^{46}$  and gas sensing.  $^{47}$  In this study, we specifically focused on TiS $_3$  in combination with  ${\rm Ti}_3{\rm C}_2{\rm T}_x$  and found that the TiS $_3$ -Ti $_3{\rm C}_2{\rm T}_x$  sensors exhibit several improved characteristics compared to the sensors based on the pristine MXene material.

 ${\rm Ti_3C_2^-T_x}$  MXene flakes were prepared using the minimally intensive layer delamination (MILD) method; <sup>28</sup> see the Experimental Section for details. Details of the materials characterization of  ${\rm Ti_3C_2T_x}$  MXene flakes from similar batches by a variety of techniques, including X-ray diffraction (XRD), X-ray photoelectron spectroscopy (XPS), Raman spectroscopy, ultraviolet—visible (UV—vis) absorption spectroscopy, and various microscopic techniques can be found in our recent publications. <sup>48–50</sup> Overall, these characterization results were standard for  ${\rm Ti_3C_2T_x}$  MXene, so here we only focus on the discussion of the data that are relevant for this sensor study. Notably, Figure 1b (left) shows an SEM image of the assynthesized  ${\rm Ti_3C_2T_x}$ , which demonstrates that the flakes were well exfoliated and over 10  $\mu$ m in lateral size.

 $TiS_3$  crystals were grown *via* a direct reaction between metallic titanium and sulfur vapor at 550 °C; see the Experimental Section. SEM image of as-prepared  $TiS_3$  whiskers is shown in Figure 1b (middle). Again, here we only focus on the discussion of the properties of  $TiS_3$  that are relevant for this sensor study, while other materials characterization by XRD, XPS, Raman spectroscopy, SEM, transmission electron microscopy (TEM), and other methods, all of which confirm

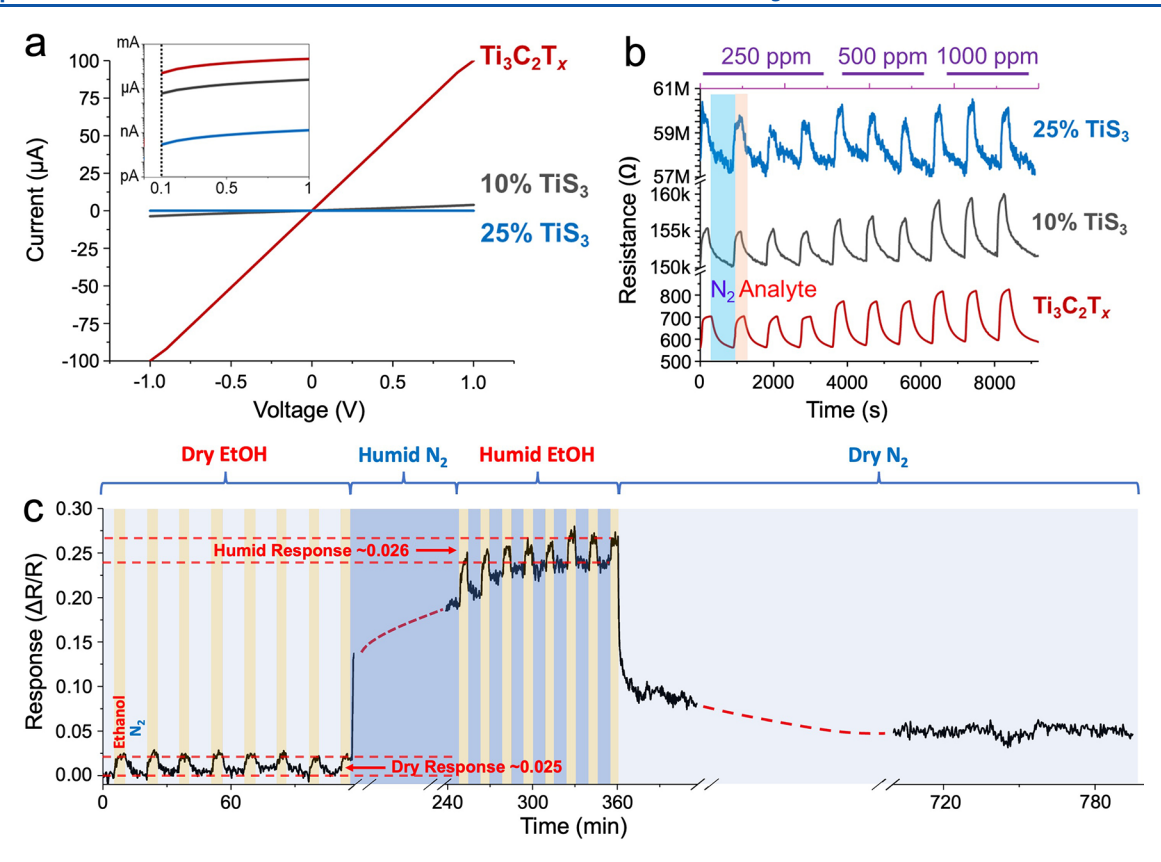


Figure 2. Room-temperature performance of  ${\rm Ti}_3{\rm C}_2{\rm T}_x$  and  ${\rm Ti}_3{\rm C}_2{\rm T}_x$ - ${\rm Ti}{\rm S}_3$  gas sensors. (a) I-V dependences for representative sensor segments with pure  ${\rm Ti}_3{\rm C}_2{\rm T}_x$ , 90 wt %  ${\rm Ti}_3{\rm C}_2{\rm T}_x$ /10 wt %  ${\rm Ti}{\rm S}_3$ , and 75 wt %  ${\rm Ti}_3{\rm C}_2{\rm T}_x$ /25 wt %  ${\rm Ti}{\rm S}_3$  device channels. The inset shows the same data on a logarithmic current scale for clarity. (b) Gas sensor responses of representative sensor segments with pure  ${\rm Ti}_3{\rm C}_2{\rm T}_x$ , 90 wt %  ${\rm Ti}_3{\rm C}_2{\rm T}_x$ /10 wt %  ${\rm Ti}{\rm S}_3$ , and 75 wt %  ${\rm Ti}_3{\rm C}_2{\rm T}_x$ /25 wt %  ${\rm Ti}_3{\rm S}_3{\rm C}_3{\rm T}_x$ /25 wt %  ${\rm Ti}_3{\rm C}_3{\rm T}_x$ /25 wt %  ${\rm Ti}_3{$ 

the high structural quality of TiS<sub>3</sub> crystals grown by the described approach, can be found in our previous works.<sup>29,51</sup>

Ti<sub>3</sub>C<sub>2</sub>T<sub>x</sub> MXene flakes were first synthesized as an aqueous suspension.<sup>28</sup> The MXene material was dried, weighed, and resuspended in dry ethanol to form a dispersion with a known concentration. In order to produce TiS<sub>3</sub> in a suspension form, bulk TiS3 whiskers were placed in ethyl acetate and sonicated for 12 h. Then, the suspension was centrifuged at 4000 rpm for 5 min to remove large particles, and a portion of the supernatant was dried to determine the concentration of suspended TiS<sub>3</sub>. The two suspensions with known concentrations were then mixed in separate vials to create 9:1 and 3:1 (by weight) Ti<sub>3</sub>C<sub>2</sub>T<sub>x</sub>-TiS<sub>3</sub> mixtures, which therefore contained 10 and 25 wt % TiS<sub>3</sub>, respectively. The Ti<sub>3</sub>C<sub>2</sub>T<sub>x</sub>-TiS<sub>3</sub> mixtures were then drop-cast from these solutions on Si/SiO2 substrates with prefabricated Ti/Pt electrodes with separations of 50  $\mu$ m and allowed to dry under ambient conditions forming a thin film. A sensor chip based on pure Ti<sub>3</sub>C<sub>2</sub>T<sub>x</sub> MXene was also prepared as a reference.<sup>10</sup> Each substrate contained 39 interdigitated Ti/Pt electrodes creating 38 independently addressable sensor channels as well as Pt thermistors and Joule heaters for in situ temperature control during sensor experiments. Sensor chips utilizing the same design were previously employed in sensor/conductivity studies of many other nanomaterials. 52-55 An individual sensor element on a chip with a dried Ti<sub>3</sub>C<sub>2</sub>T<sub>x</sub>-TiS<sub>3</sub> film bridging two Ti/Pt electrodes is schematically shown in Figure 1a. Figure 1b (right) shows an SEM image of a dried film containing 75 wt % Ti<sub>3</sub>C<sub>2</sub>T<sub>x</sub> and 25 wt % TiS<sub>3</sub>, in which the wrinkled 2D MXene

flakes and the solution-exfoliated 1D TiS<sub>3</sub> nanoribbons are easily recognizable because their different morphologies. After the deposition, each chip was loaded into a home-built gas sensor testing chamber for *in situ* analysis and annealing treatment; see the Experimental Section. During sensor experiments, we generated ppm-level mixtures of ethanol vapors in nitrogen and monitored the conductivity of the segments individually as the atmosphere was varied relative to a pure nitrogen background when the mixture was flowed over a sensor chip.

The basic electronic properties of both materials, individually, have been well characterized in previous reports. Electrical measurements performed on Ti<sub>3</sub>C<sub>2</sub>T<sub>x</sub> MXene films and individual flakes revealed their metallic properties and high conductivities exceeding 10,000 S/cm. 56,57 In contrast, experimental studies of TiS3 revealed its semiconductor character<sup>30-37,42-44</sup> with substantially lower electrical conductivities, which were reported in a wide range from  $5 \times 10^{-5}$ to 0.5 S/cm depending on the material embodiment (single crystals, printed films, etc.). 41,42,45,46 Therefore, the incorporation of TiS<sub>3</sub> into Ti<sub>3</sub>C<sub>2</sub>T<sub>x</sub> MXene films was expected to decrease their electrical conductivity, which we observed experimentally (Figure 2a). According to the device architecture presented in this work (Figure 1a), the current (I)-voltage (V) dependences were measured across two Ti/Pt electrodes separated by a 50  $\mu$ m channel of a chemiresistive film. The sensor segments covered with pure Ti<sub>3</sub>C<sub>2</sub>T<sub>x</sub> MXene films exhibited linear room-temperature I-V dependencies with currents of about 100  $\mu$ A at a bias of 1 V. With 10 wt %

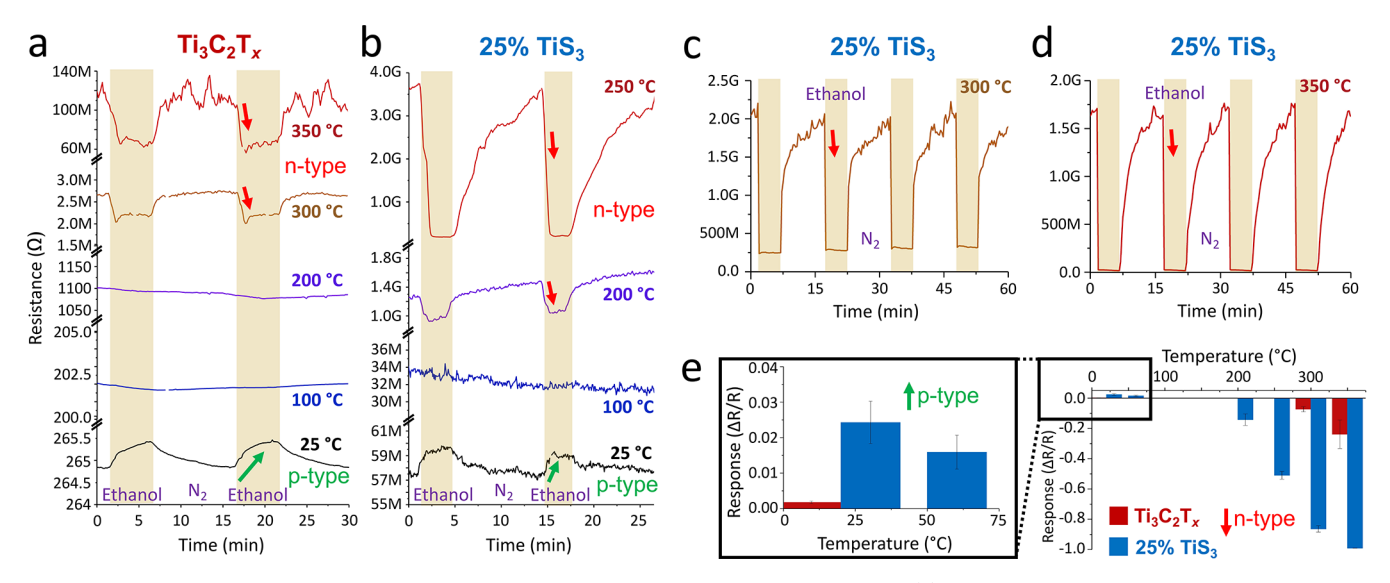


Figure 3. Temperature-dependent sensing behavior of  $Ti_3C_2T_x$  and  $Ti_3C_2T_x$ - $TiS_3$  gas sensors. (a) Temperature-dependent sensor response of a representative pristine  $Ti_3C_2T_x$  device to 500 ppm ethanol vapors in nitrogen. (b) Temperature-dependent sensor response of a representative 75 wt %  $Ti_3C_2T_x/25$  wt %  $TiS_3$  device to 500 ppm ethanol vapors in nitrogen in the temperature range of 25–250 °C. (c, d) Ethanol (500 ppm) sensing with a different 75 wt %  $Ti_3C_2T_x/25$  wt %  $TiS_3$  device at (c) 300 and (d) 350 °C, showing further increase in the sensor responses with temperature and reproducibility of the cycles. (e) Temperature-dependent response values ( $\Delta R/R$ ) for the two film compositions shown in (a–d).

 $TiS_3$ , the channel currents dropped by about 2 orders of magnitude, and a further decrease in conductivity was observed for MXene films with 25 wt %  $TiS_3$ ; see the I-V curves for representative devices in Figure 2a. Because of this pronounced current decrease, we did not test  $Ti_3C_2T_x$ - $TiS_3$  compositions with  $TiS_3$  content exceeding 25 wt %.

Figure 2b shows the effect of the TiS<sub>3</sub> loading on the roomtemperature sensor response of  $Ti_3C_2T_x$  MXene films to ppmconcentrations of ethanol, which was used as a model analyte. As was reported in previous studies on chemiresistive gas sensors based on  $Ti_3C_2T_x$  films, <sup>9,11</sup> the adsorption of analyte molecules increases their resistance, which we observed for the MXene devices fabricated in this study as well. When TiS<sub>3</sub> is incorporated into the films, their resistance increases but the sensor response remains qualitatively the same; see Figure 2b. Interestingly, sensors based on pure TiS<sub>3</sub> also exhibit resistance increase upon their exposure to alcohols, <sup>47</sup> so in Ti<sub>3</sub>C<sub>2</sub>T<sub>x</sub>-TiS<sub>3</sub> devices both components contribute to the observed sensor response at room temperature. The 75 wt %  $Ti_3C_2T_x/25$  wt % TiS<sub>3</sub> sensors showed a stable response to ethanol over the course of several days, as illustrated in Figure S1 in the Supporting Information.

While in this study we primarily focused on the sensing responses to the analytes vs the dry nitrogen background, the devices were also functional in the presence of humidity, as illustrated in Figure 2c. In this experiment, we tested the response of the 75 wt %  $Ti_3C_2T_x/25$  wt %  $TiS_3$  sensor to 500 ppm of ethanol. First, we measured several cycles of response of the sensor to ethanol in dry nitrogen, then the sensor was exposed to humid nitrogen with a relative humidity (RH) of about 25%, and in the following measurements, the sensor was cyclically exposed to humid ethanol and purged with humid nitrogen, both with ~25% RH. Figure 2c shows that although the humidity increased the background resistance, likely due to the intercalation of water molecules in the Ti<sub>3</sub>C<sub>2</sub>T<sub>x</sub>-TiS<sub>3</sub> composite, the sensor responses in dry and humid conditions were comparable. This observation is consistent with the previously reported stability of the room-temperature sensor

response of another MXene composite sensor based on  ${\rm Ti_3C_2T_x\text{-}WO_3.}^{25}$  When the device was finally purged with dry nitrogen, the background resistance slowly decreased toward the original levels (Figure 2c).

The effect of TiS<sub>3</sub> loading on the behavior of MXene gas sensors is even more pronounced upon their annealing. Figure 3a summarizes the temperature-dependent sensing behavior of gas sensors based on Ti<sub>3</sub>C<sub>2</sub>T<sub>x</sub> MXene films. The sensors exhibit a highly tunable response to ethanol, as the resistance increases upon their exposure to ethanol molecules at room temperature (p-type response) but decreases if the sensors were annealed at ≥300 °C (n-type response). As was demonstrated by Pazniak et al., this temperature-dependent sensor response is caused by the partial oxidation of Ti<sub>3</sub>C<sub>2</sub>T<sub>r</sub> MXene and the formation of TiO<sub>2</sub> nanoparticles. <sup>10</sup> At room temperature, the pristine  $Ti_3C_2T_x$  sensors exhibit the expected p-type response, but once TiO<sub>2</sub> nanoparticles form in appreciable amounts after high-temperature annealing, their intrinsic n-type sensing response overcomes the response of the remaining MXene material. The formation of local heterojunctions between the semiconducting TiO2 nanoparticles and the metallic Ti<sub>3</sub>C<sub>2</sub>T<sub>x</sub> is also expected to contribute to the improved sensing response of MXene upon annealing. At intermediate annealing temperatures, when the degree of MXene oxidation is small, the opposite responses of TiO<sub>2</sub> and Ti<sub>3</sub>C<sub>2</sub>T<sub>x</sub> effectively cancel each other so that the resulting material exhibits no response to ethanol upon annealing at 100 and 200 °C; see Figure 3a. Overall, the data in Figure 3a demonstrate that Ti<sub>3</sub>C<sub>2</sub>T<sub>r</sub> MXene provides a highly tunable sensing platform, in which the direction of the response can be engineered simply by the annealing temperature.10

Figure 3b–d demonstrates that the incorporation of  $TiS_3$  into MXene films improves their sensor characteristics. First, the presence of  $TiS_3$  decreases the temperature of the p- to n-type transition of the sensing response by about 100 °C. While the sensors based on pristine  $Ti_3C_2T_x$  show no response to 500 ppm ethanol at 200 °C (Figure 3a), the sensors with 25 wt %

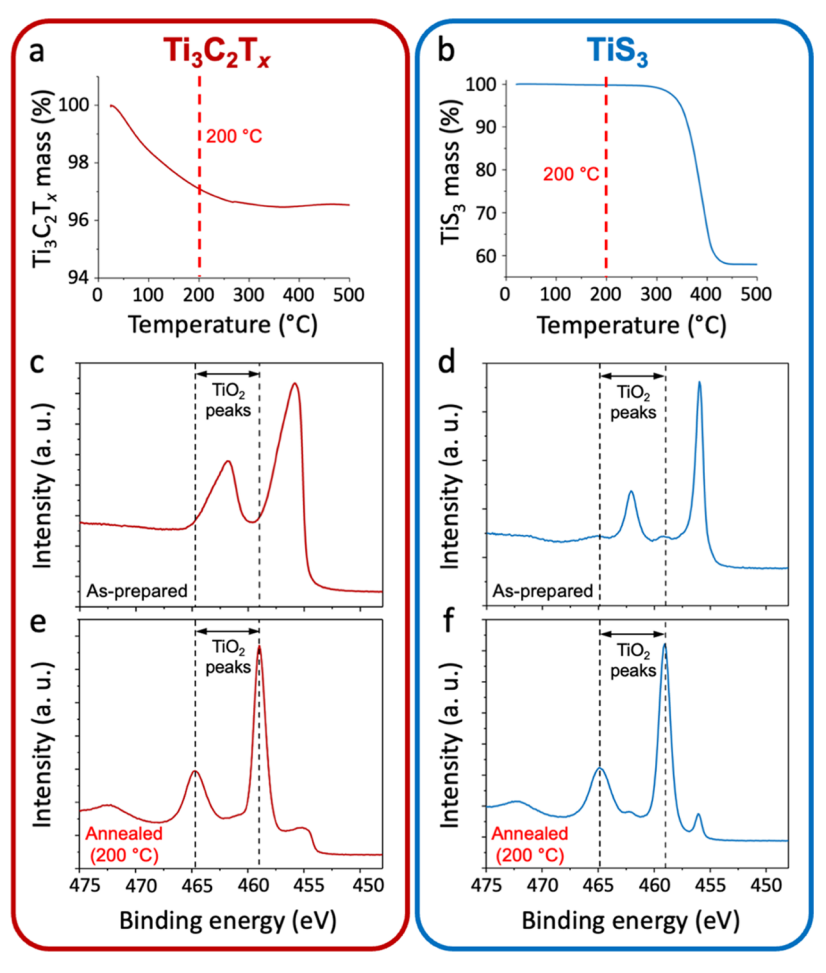


**Figure 4.** Analysis of the oxidation of  $\text{Ti}_3\text{C}_2\text{T}_x$  and  $\text{TiS}_3$  upon annealing. (a) TGA curve showing oxidation behavior of  $\text{Ti}_3\text{C}_2\text{T}_x$  as it is heated from room temperature to 500 °C. (b) TGA curve showing oxidation behavior of  $\text{TiS}_3$  as it is heated from room temperature to 500 °C. (c–f) Comparative XPS Ti 2p spectra of individual materials,  $\text{Ti}_3\text{C}_2\text{T}_x$  and  $\text{TiS}_3$ , before and after annealing at 200 °C. The vertical dashed lines show the positions of the Ti 2p signals for  $\text{TiO}_2$ .

TiS<sub>3</sub> already show the n-type response at this temperature (Figure 3b). For pristine MXene devices, the n-type response is not observed until the sensors are annealed at 300 °C. Second, the  $Ti_3C_2T_x$ - $TiS_3$  gas sensors exhibited greater sensing responses compared to their pure MXene counterparts, as shown in Figure 3e. This graph presents the current modulation in terms of sensing response, which is defined as  $(R_a - R_0)/R_0$ , where  $R_a$  is the resistance of the segment under analyte atmosphere, and  $R_0$  is the resistance of the segment under an N2 atmosphere. By this convention, a positive response corresponds to p-type sensing behavior as shown by the 25 °C data in Figure 3e. The sensing response of the hybrid film outperforms that of the pristine MXene film at all tested temperatures. Additionally, since the highest tested operation temperature for each film resulted in the highest sensing response, it is likely that the trend continues even beyond the temperature ranges reported here. While the data in Figure 3e illustrate the temperature-dependent p-n transition of the sensor response of a 75 wt % Ti<sub>3</sub>C<sub>2</sub>T<sub>x</sub>/25 wt % TiS<sub>3</sub> composite to 500 ppm ethanol, similar transitions were observed for other analyte concentrations, such as 250 and 1000 ppm; see Figure S2a in the Supporting Information. Also, while this study primarily focused on ethanol as a model analyte, other low-molecular-weight alcohols, such as methanol and isopropanol, demonstrated a similar behavior in these

experiments, exhibiting an n-type response at temperatures above 200 °C (Figure S2b) if sensed by a 75 wt %  $Ti_3C_2T_x/25$  wt %  $TiS_3$  device.

The improved n-type sensing response of the  $Ti_3C_2T_x$ - $TiS_3$ devices upon annealing is rationalized by the formation of intimate contact between the metallic Ti<sub>3</sub>C<sub>2</sub>T<sub>x</sub> MXene and the semiconducting TiO<sub>2</sub> (which is expected to form on the surface of TiS<sub>3</sub> particles), as has been discussed for previously reported composite gas sensors between MXene and TiO<sub>2</sub>. <sup>10,18</sup> Due to the small size of TiO2 particles formed by the mild annealing conditions, they are expected to be fully depleted. 10 During operation at high temperatures, reactions with surfaceadsorbed oxygen species govern the width of these depletion regions, which affects electron transport through the film.<sup>58</sup> The p-type sensing response of the MXene gas sensors at room temperature is also improved by the addition of TiS<sub>3</sub> (Figure 3e). At room temperature, both  $Ti_3C_2T_x$  and  $TiS_3$  exhibit an increase in resistance on exposure to alcohols, 9,10,47 so these materials work collectively in composite Ti<sub>3</sub>C<sub>2</sub>T<sub>x</sub>-TiS<sub>3</sub> sensor devices.

Since the proposed sensing mechanism, in particular the change from p- to n-type response upon annealing, relies on the formation of  ${\rm TiO}_2$ , it is important to establish the degree of oxidation of  ${\rm Ti}_3{\rm C}_2{\rm T}_x$  and  ${\rm TiS}_3$  within the studied temperature range. We investigated the oxidation of both materials by a

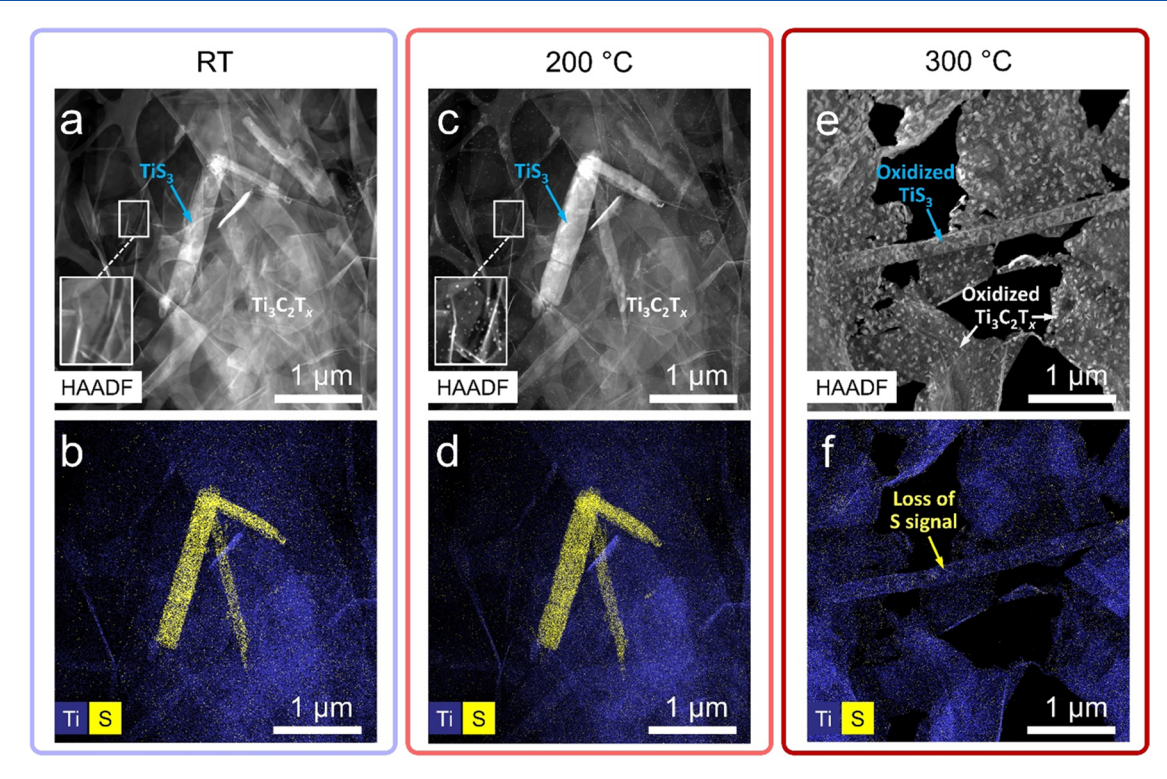


Figure 5. STEM/EDX analysis of materials in response to annealing. (a, b) HAADF image and EDX map (Ti and S) for a freshly prepared 75 wt %  $Ti_3C_2T_x/25$  wt %  $TiS_3$  composite. (c, d) HAADF image and EDX map for the same location after annealing at 200 °C for 3 h. (e, f) HAADF image and EDX map for another location on the same TEM grid after annealing at 300 °C for 3 h.

combination of thermogravimetric analysis (TGA), X-ray photoelectron spectroscopy (XPS), as well as scanning transmission electron microscopy (STEM) in a high-angle annular dark-field (HAADF) imaging mode and elemental mapping by energy-dispersive X-ray (EDX) spectroscopy. TGA enables monitoring the bulk transition of either  $\mathrm{Ti_3C_2T_x}$  or  $\mathrm{TiS_3}$  to  $\mathrm{TiO_2}$ , as both of these oxidation reactions are accompanied by a mass change of a solid sample. In contrast, XPS has a very small depth of analysis and allows probing the surface oxidation of  $\mathrm{Ti_3C_2T_x}$  or  $\mathrm{TiS_3}$ . Therefore, these characterization techniques provide complimentary information on the formation of  $\mathrm{TiO_2}$  upon annealing of these materials. STEM and EDX provide information about the morphology and elemental composition of each material as a function of annealing treatment.

Figure 4a,b shows the TGA curves for  $Ti_3C_2T_x$  and  $TiS_3$ , respectively; Figure S3 also provides TGA data for a 75 wt %  $Ti_3C_2T_x/25$  wt %  $TiS_3$  composite. Of particular interest for the sensor data is the temperature of 200 °C, at which the Ti<sub>3</sub>C<sub>2</sub>T<sub>x</sub>-TiS<sub>3</sub> devices show a transition from p- to n-type response (Figure 3b), suggesting that at this annealing stage, a sufficient amount of TiO2 already formed to overcome the original room-temperature response of the sensors. Interestingly, neither material shows any signs of bulk oxidation based on the TGA data (Figure 4a,b). Ti<sub>3</sub>C<sub>2</sub>T<sub>x</sub> MXene was previously studied by a combined TGA and mass spectrometry analysis to correlate the observed mass loss with evolution of volatile reaction products. 10 It was demonstrated that Ti<sub>3</sub>C<sub>2</sub>T<sub>x</sub> first loses mass due to the removal of the adsorbed water and some of the surface functionalities and then, above ~350 °C, there is a mass increase because of the MXene oxidation according to the net reaction

$$Ti_3C_2(s) + 5O_2(g) \xrightarrow{\Delta} 3TiO_2(s) + 2CO_2(g) + heat$$

As a result of this reaction, the sample mass increases because 3 moles of  ${\rm TiO_2}$  weighs more than 1 mole of  ${\rm Ti_3C_2}$ . The TGA curve in Figure 4a is in agreement with these previous observations. The temperature of interest, 200 °C, which is marked by the vertical red line in Figure 4a, is below the onset of the mass increase at 350 °C corresponding to the active oxidation of  ${\rm Ti_3C_2T_x}$ . Therefore, there is no bulk oxidation of MXene upon annealing at 200 °C, and the material primarily remains as titanium carbide.

A similar conclusion can be drawn for  $TiS_3$  based on the TGA curve in Figure 4b. The figure shows that the mass loss starts around 300 °C, <sup>59</sup> corresponding to the net reaction

$$TiS_3(s) + 4O_2(g) \xrightarrow{\Delta} TiO_2(s) + 3SO_2(g) + heat$$

No noticeable mass loss is observed at 200 °C, suggesting there is no bulk oxidation of  $\mathrm{TiS}_3$  at this temperature. From the comparison of Figure 4a,b, it is also clear that  $\mathrm{TiS}_3$  is less thermally stable than  $\mathrm{Ti}_3\mathrm{C}_2\mathrm{T}_x$ . Significant conversion of  $\mathrm{TiS}_3$  to  $\mathrm{TiO}_2$  is shown at temperatures around 300–350 °C by a sharp decrease in mass, <sup>59</sup> while temperatures above 350–400 °C are needed before the onset of  $\mathrm{Ti}_3\mathrm{C}_2\mathrm{T}_x$  oxidation as shown by a mass increase. <sup>10</sup> With a further increase in temperature  $\mathrm{TiS}_3$  completely converts to  $\mathrm{TiO}_2$  at about 425 °C if heated with a constant rate of 10 °C/min, as in the TGA experiment (Figure 4b), while the conversion of  $\mathrm{Ti}_3\mathrm{C}_2\mathrm{T}_x$  to  $\mathrm{TiO}_2$  completes at even higher temperatures for the same annealing procedure (Figure 4a). <sup>10</sup>

While both materials,  $Ti_3C_2T_x$  and  $TiS_3$ , retain their bulk chemical composition upon annealing at 200 °C, XPS analysis demonstrates their strong surface oxidation; see Figure 4c–f. We measured the high-resolution XPS Ti 2p spectra of each

material before and after annealing at 200 °C for 3 h. In Figure 4c-f, the vertical dashed lines located at 459.0 and 464.7 eV correspond to the spectral positions of Ti  $2p_{3/2}$  and Ti  $2p_{1/2}$ peaks of  $Ti^{4+}$  in  $TiO_2^{60-62}$  which also has a characteristic satellite in the area from 470 to 475 eV. The XPS Ti 2p spectrum of the as-prepared MXene in Figure 4c demonstrates that there are no pronounced peaks at these binding energies, suggesting the high quality of the Ti<sub>3</sub>C<sub>2</sub>T<sub>x</sub> sample. The spectrum predominantly consists of characteristic Ti 2p peaks centered at 455.9 eV (Ti  $2p_{3/2}$ ) and 461.8 eV (Ti  $2p_{1/2}$ ), which are consistent with the previous studies of Ti<sub>3</sub>C<sub>2</sub>T<sub>x</sub> MXene.<sup>60</sup> However, the XPS Ti 2p spectrum in Figure 4e shows the emergence of the characteristic TiO<sub>2</sub> peaks upon annealing of the sample at 200 °C. Figure 4d shows the XPS Ti 2p spectrum of as-prepared TiS<sub>3</sub> with peaks located at 456.0 eV (Ti  $2p_{3/2}$ ) and 462.1 eV (Ti  $2p_{1/2}$ ), and in a similar way, after annealing the surface of the TiS<sub>3</sub> is converted to TiO<sub>2</sub> (Figure 4f). For both materials, the characteristic satellite peak of Ti<sup>4+</sup> in TiO<sub>2</sub> in the area from 470 to 475 eV emerges in the XPS Ti 2p spectra after the annealing; see Figure 4e,f.

Overall, the TGA and XPS data are in good agreement with the results of sensor measurements. Within the studied temperature range, both Ti<sub>3</sub>C<sub>2</sub>T<sub>x</sub> and TiS<sub>3</sub> oxidize on surface, although the amounts of the produced TiO<sub>2</sub> are relatively small such that they are not detectable by TGA. The amount of TiO<sub>2</sub> produced on the surface of pristine Ti<sub>3</sub>C<sub>2</sub>T<sub>x</sub> upon annealing at 200 °C is not sufficient to convert the MXene sensor response from p- to n-type (Figure 3a). The additional amount of TiO<sub>2</sub> that is necessary for such conversion can be provided by TiS<sub>3</sub> additive in Ti<sub>3</sub>C<sub>2</sub>T<sub>x</sub>-TiS<sub>3</sub> composite sensors (Figure 3b). The TiS<sub>3</sub> nanoribbons retain their bulk composition upon annealing at 200 °C, but their surface oxidizes by the in situ annealing during the sensing experiments, which provides TiO<sub>2</sub> in intimate contact with Ti<sub>3</sub>C<sub>2</sub>T<sub>r</sub> MXene. Additionally, the disparity of oxidation behavior between Ti<sub>3</sub>C<sub>2</sub>T<sub>x</sub> and TiS<sub>3</sub> explains the results shown in Figure 3, as  $TiS_3$  is oxidized more readily causing a qualitative change to the gas sensing mechanism and response at a lower temperature than the pristine  $Ti_3C_2T_r$  film.

To visualize the oxidation of the Ti<sub>3</sub>C<sub>2</sub>T<sub>x</sub>-TiS<sub>3</sub> composite, we also followed the evolution of each material microscopically; see Figures 5 and S4. The fresh, unannealed sample contains high-quality Ti<sub>3</sub>C<sub>2</sub>T<sub>x</sub> flakes and TiS<sub>3</sub> nanoribbons, which can be recognized by their 2D and 1D shapes, respectively (Figure 5a). Additionally, the TiS<sub>3</sub> nanoribbons can be distinguished by the S signal in the EDX map (Figure 5b). After annealing at 200 °C (Figure 5c,d), the  $Ti_3C_2T_x$ flakes generally retain their morphology, although a close inspection of TEM images reveals the formation of small TiO<sub>2</sub> nanoparticles (compare the insets in Figure 5a,5c that show the same area before and after annealing). Contrastingly, in the case of TiS<sub>3</sub>, the dimensions of the nanoribbon have swelled considerably as a thin layer of TiO2 now covers the surface of the entire crystal, rather than an abundance of small, scattered particles. This morphology of TiO<sub>2</sub> growth on TiS<sub>3</sub> is in agreement with previous reports on the thermal decomposition of this material.<sup>59</sup> At this temperature, the bulk of TiS<sub>3</sub> remains unaffected, as shown by the strong S signal that is still present in the EDX map in Figure 5d. The same conclusions have been drawn from the data shown in Figure 4, which demonstrate that at 200 °C the oxidation of TiS3 occurs only on a surface (XPS) but not in bulk (TGA).

After annealing to even higher temperatures (300 °C, Figure 5e,f), the oxidation of both materials is much more dramatic, in agreement with the TGA results (Figure 4a,b). Due to the degradation of the amorphous carbon support film of a TEM grid, we could not image the same area of the sample as in Figure 5a–d. However, imaging of a different area of the composite shows severe oxidation, which is clear by the presence of large  $TiO_2$  particles on  $Ti_3C_2T_x$  sheets (Figure 5e) and the complete loss of S signal from a  $TiS_3$  nanoribbon in the EDX map (Figure 5f). Overall, the results of STEM and EDX for a  $Ti_3C_2T_x$ - $TiS_3$  composite corroborate the conclusions drawn from the analysis of TGA and XPS data.

### CONCLUSIONS

Herein, we have demonstrated the effect of TiS<sub>3</sub> co-deposition on the temperature-dependent sensing properties of a  $Ti_3C_2T_x$ based MXene gas sensor. Building on the previous work with partially oxidized Ti<sub>3</sub>C<sub>2</sub>T<sub>r</sub> films as gas sensors, herein we report on the partial thermal oxidation of a  $TiS_3$ - $Ti_3C_2T_x$  hybrid film to the same end. The addition of TiS<sub>3</sub> into the deposition solution imparts many favorable properties to the sensing film including intrinsic semiconductor heterojunctions and an alternative TiO<sub>2</sub> source with lower thermal stability. Annealing such a film allows for the general preservation of MXene as the sensor material while also providing the benefits of heterojunctions with TiO<sub>2</sub> nanoparticles formed from the oxidation of TiS<sub>3</sub> below 350 °C. The presence of TiO<sub>2</sub> particles formed by the additive, TiS3, induces a qualitative change to the sensor response from p- to n-type as well as a quantitative improvement of important sensing parameters such as response magnitude and response time for sensing lowmolecular-weight alcohols.

Such a sensor morphology hopes to bridge the knowledge gap between the novel MXene gas sensor and the well-characterized semiconducting-oxide gas sensors which are widely used and commercially viable. The described strategy provides a general approach toward the improvement of chemiresistive gas sensors based on conductive MXenes that should be applicable to a variety of MXene compositions and additives, many of which remain unstudied. This work also provides some insight into the mechanism of oxidation and the gas sensor response of composite films with 2D MXenes.

## EXPERIMENTAL SECTION

**Synthesis of TiS**<sub>3</sub>. TiS<sub>3</sub> whiskers were synthesized as described in ref 29. A small piece of 0.25-mm-thick titanium foil (99.99+%, Alfa Aesar) and a stoichiometric excess of sulfur powder (Sigma-Aldrich) were placed at opposite ends of a quartz ampoule evacuated down to  $\sim\!200$  mTorr. The ampoule was then placed in a tube furnace, with the Ti foil end of the ampoule placed directly in the center, in the hottest zone of the furnace, which establishes a small temperature gradient across the ampoule. The reagents were then heated to 550 °C at a ramp rate of 10 °C/min and allowed to react for about 2 weeks as TiS<sub>3</sub> crystallizes on the Ti foil and the walls of the quartz ampoule. After this time, the furnace was cooled to room temperature and the needle-like TiS<sub>3</sub> crystals were harvested.

**Synthesis of Ti<sub>3</sub>C<sub>2</sub>T<sub>x</sub> MXene.** Ti<sub>3</sub>AlC<sub>2</sub> MAX phase was synthesized according to our previous report. Ti (99%, 325 mesh, Alfa Aesar), TiC (99.9%, 325 mesh, Alfa Aesar) were mixed using a pestle and mortar at a 1:2:1.2 molar ratio, transferred into an alumina crucible, and annealed at 1450 °C for 8 h while continuously purged with argon (300 sccm). After annealing, the prepared MAX phase was crushed and sieved to collect particles with sizes between 25 and 40  $\mu$ m. Ti<sub>3</sub>C<sub>2</sub>T<sub>x</sub> MXene was then synthesized from the MAX phase using the MILD method. In a

typical synthesis, 3 g of  $\rm Ti_3AlC_2$  MAX phase powder was slowly added to a 60 mL mixture of 9 M HCl (VWR) and 4.8 g of LiF (Spectrum Chemical) and etched for 24 h. After etching, the sample was thoroughly washed with deionized water until the pH reached around 6 and the MXene had delaminated into predominantly monolayer flakes. The aqueous  $\rm Ti_3C_2T_x$  solution was kept under nitrogen in a refrigerator at 4 °C for further experiments.

SEM. Scanning electron microscopy of  $Ti_3C_2T_x$  MXene,  $TiS_3$ , and composite films was performed using an FEI Nova NanoSEM 450 scanning electron microscope with an accelerating voltage of 5 kV. A small amount of solution was deposited on a  $Si/SiO_2$  substrate, dried in air, and loaded into the instrument.

XPS. The surface composition of  $\mathrm{Ti_3C_2T_x}$  and  $\mathrm{TiS_3}$  was analyzed at room temperature via a Thermo Scientific K $\alpha$ X-ray photoelectron spectrometer using a monochromated Al K $\alpha$  (1486.6 eV) X-ray source. The samples were mounted onto conductive copper tape, and a low-energy electron flood gun was used for charge neutralization. The high-resolution spectra of Ti 2p were collected using a pass energy of 20 eV and a 0.1 eV step.

*TGA*. Thermal analysis of the materials was performed using a TA Instruments TGA 550 with a ramp rate of 10  $^{\circ}$ C/min and experiment details as described in the main text.

*TEM.* The evolution of the materials with annealing was investigated microscopically on an FEI Tecnai Osiris transmission electron microscope equipped with a HAADF detector and an X-FEG high-brightness Schottky field emission gun. The accelerating voltage was 200 kV. For (S)TEM characterization, a sample of  ${\rm Ti}_3{\rm C}_2{\rm T}_x$ - ${\rm Ti}{\rm S}_3$  composite was diluted in ethanol, and then the suspension was dropcast on a lacey carbon-coated Cu TEM grid.

**Electrical Characterization.** Basic electrical characterization was performed inside a LakeShore TTPX 4-probe vacuum probe station in conjunction with an Agilent 4155C semiconductor parameter analyzer.

**Sensor Experiments.** Sensor experiments were conducted in a home-built gas sensor system  $^{52}$  with flow controlled by several MKS mass flow controllers (MFCs). As discussed in the main text, the sensor chip consisted of many pairs of interdigitated Ti/Pt electrodes, separated by 50  $\mu$ m channels over Si/SiO<sub>2</sub> substrate. Before the deposition of the sensing material, this substrate was wire bonded to a chip carrier with gold wire (99.995%, 0.002" diameter; Alfa Aesar) using a West-Bond manual ultrasonic wedge bonder. After fabrication of the sensing film, the chip carrier could be interfaced with the electronic analysis equipment and mounted into the sensing chamber.

A National Instrument LabVIEW program was developed to control the data collection process. A Keithley 7001 switch system was used for sequential, independent monitoring of the resistance between each pair of electrodes. The electrical resistance of the film was measured by an Agilent 4155C semiconductor parameter analyzer as a function of time to varying atmospheres.

Different vapor environments were created with the use of homemade capillary diffusion vials. When the reservoir of such a vial is filled with a volatile analyte, it evaporates to fill the vial with saturated vapors. Therefore, a gas-phase concentration gradient exists between the inside and the outside of the vial that is only accessible by diffusion through the capillary. The diffusion rate of the analyte out of the vial is dependent on the inner diameter and length of the diffusion pathway (i.e., the capillary) as well as the temperature. So, at a constant temperature, the atmosphere inside the sensing chamber can be engineered by flowing pure N<sub>2</sub> as a diluent past the vapors exiting the capillary. The diffusing vapors are carried by the diluent, and the equilibrium is maintained through the capillary. A larger diluent flow results in a lower concentration of analyte and vice versa, so the resulting atmosphere can be controlled by MFCs determining the flow of diluent. Regardless of diluent flow, an exhaust port is used to bleed off all but 25 sccm (controlled by MFC) so that the effect of flow rate is not included in the sensing response. During the recovery phase of the sensing response, the chamber containing the diffusion vial is continuously purged to prevent accumulation of analyte, which could result in overestimation of the target atmosphere as well as affect the established equilibrium.

#### ASSOCIATED CONTENT

# **Solution** Supporting Information

The Supporting Information is available free of charge at https://pubs.acs.org/doi/10.1021/acsanm.3c00788.

Room-temperature stability of  $Ti_3C_2T_x$ - $TiS_3$  sensors (Figure S1); concentration-dependent response of  $Ti_3C_2T_x$ - $TiS_3$  sensors to low-molecular-weight alcohols (Figure S2); comparison of TGA curves for  $Ti_3C_2T_x$ ,  $TiS_3$ , and  $Ti_3C_2T_x$ - $TiS_3$  composite (Figure S3); bright-field TEM image of a  $Ti_3C_2T_x$ - $TiS_3$  composite material at room temperature and after annealing at 200 and 300 °C (Figure S4) (PDF)

#### AUTHOR INFORMATION

## **Corresponding Author**

Alexander Sinitskii — Department of Chemistry, University of Nebraska-Lincoln, Lincoln, Nebraska 68588, United States; Nebraska Center for Materials and Nanoscience, University of Nebraska-Lincoln, Lincoln, Nebraska 68588, United States; orcid.org/0000-0002-8688-3451; Email: sinitskii@unl.edu

#### Authors

Michael J. Loes — Department of Chemistry, University of Nebraska-Lincoln, Lincoln, Nebraska 68588, United States Saman Bagheri — Department of Chemistry, University of Nebraska-Lincoln, Lincoln, Nebraska 68588, United States; orcid.org/0000-0002-4206-3021

Nataliia S. Vorobeva — Department of Chemistry, University of Nebraska-Lincoln, Lincoln, Nebraska 68588, United States Jehad Abourahma — Department of Chemistry, University of Nebraska-Lincoln, Lincoln, Nebraska 68588, United States

Complete contact information is available at: https://pubs.acs.org/10.1021/acsanm.3c00788

# **Author Contributions**

M.J.L. performed the device fabrication and sensor measurements. S.B. synthesized and characterized  $\mathrm{Ti}_3\mathrm{C}_2\mathrm{T}_x$  MXene as well as performed electron microscopy. J.A. synthesized and characterized  $\mathrm{Ti}\mathrm{S}_3$ . N.S.V. performed the XPS analysis. M.J.L. and A.S. wrote the manuscript. A.S. conceived the idea of this study and supervised the project.

## **Notes**

The authors declare no competing financial interest.

#### ACKNOWLEDGMENTS

This work was supported by the Nebraska Center for Energy Sciences Research (NCESR) and the National Science Foundation (NSF) through EPSCoR RII Track-1: Emergent Quantum Materials and Technologies (EQUATE), award OIA-2044049. The device fabrication was performed using the instrumentation at the Nebraska Nanoscale Facility, which is supported by the NSF (ECCS-2025298) and the Nebraska Research Initiative.

#### REFERENCES

- (1) Gogotsi, Y.; Anasori, B. The Rise of MXenes. ACS Nano 2019, 13, 8491-8494.
- (2) Halim, J.; Cook, K. M.; Naguib, M.; Eklund, P.; Gogotsi, Y.; Rosen, J.; Barsoum, M. W. X-ray photoelectron spectroscopy of select multi-layered transition metal carbides (MXenes). *Appl. Surf. Sci.* **2016**, 362, 406–417.

- (3) Seredych, M.; Shuck, C. E.; Pinto, D.; Alhabeb, M.; Precetti, E.; Deysher, G.; Anasori, B.; Kurra, N.; Gogotsi, Y. High-Temperature Behavior and Surface Chemistry of Carbide MXenes Studied by Thermal Analysis. *Chem. Mater.* **2019**, *31*, 3324–3332.
- (4) Jian, Y.; Qu, D.; Guo, L.; Zhu, Y.; Su, C.; Feng, H.; Zhang, G.; Zhang, J.; Wu, W.; Yao, M.-S. The prior rules of designing  $\mathrm{Ti}_3\mathrm{C}_2\mathrm{T}_x$  MXene-based gas sensors. Front. Chem. Sci. Eng. 2021, 15, 505–517.
- (5) Bhardwaj, R.; Hazra, A. MXene-based gas sensors. J. Mater. Chem. C 2021, 9, 15735–15754.
- (6) Kim, S. J.; Choi, J.; Maleski, K.; Hantanasirisakul, K.; Jung, H.-T.; Gogotsi, Y.; Ahn, C. W. Interfacial Assembly of Ultrathin, Functional MXene Films. *ACS Appl. Mater. Interfaces* **2019**, *11*, 32320–32327.
- (7) Lee, E.; Kim, D.-J. Review— Recent Exploration of Two-Dimensional MXenes for Gas Sensing: From a Theoretical to an Experimental View. *J. Electrochem. Soc.* **2020**, *167*, No. 037515.
- (8) Zhang, C. J.; Pinilla, S.; McEvoy, N.; Cullen, C. P.; Anasori, B.; Long, E.; Park, S.-H.; Seral-Ascaso, A.; Shmeliov, A.; Krishnan, D.; Morant, C.; Liu, X.; Duesberg, G. S.; Gogotsi, Y.; Nicolosi, V. Oxidation Stability of Colloidal Two-Dimensional Titanium Carbides (MXenes). *Chem. Mater.* **2017**, 29, 4848–4856.
- (9) Kim, S. J.; Koh, H.-J.; Ren, C. E.; Kwon, O.; Maleski, K.; Cho, S.-Y.; Anasori, B.; Kim, C.-K.; Choi, Y.-K.; Kim, J.; Gogotsi, Y.; Jung, H.-T. Metallic Ti<sub>3</sub>C<sub>2</sub>T<sub>x</sub> MXene Gas Sensors with Ultrahigh Signal-to-Noise Ratio. *ACS Nano* **2018**, *12*, 986–993.
- (10) Pazniak, H.; Plugin, I. A.; Loes, M. J.; Inerbaev, T. M.; Burmistrov, I. N.; Gorshenkov, M.; Polcak, J.; Varezhnikov, A. S.; Sommer, M.; Kuznetsov, D. V.; Bruns, M.; Fedorov, F. S.; Vorobeva, N. S.; Sinitskii, A.; Sysoev, V. V. Partially Oxidized Ti<sub>3</sub>C<sub>2</sub>T<sub>x</sub> MXenes for Fast and Selective Detection of Organic Vapors at Part-per-Million Concentrations. *ACS Appl. Nano Mater.* **2020**, *3*, 3195–3204.
- (11) Lee, E.; VahidMohammadi, A.; Prorok, B. C.; Yoon, Y. S.; Beidaghi, M.; Kim, D.-J. Room Temperature Gas Sensing of Two-Dimensional Titanium Carbide (MXene). *ACS Appl. Mater. Interfaces* **2017**, *9*, 37184–37190.
- (12) Chen, W. Y.; Jiang, X.; Lai, S.-N.; Peroulis, D.; Stanciu, L. Nanohybrids of a MXene and transition metal dichalcogenide for selective detection of volatile organic compounds. *Nat. Commun.* **2020**, *11*, No. 1302.
- (13) Ama, O.; Sadiq, M.; Johnson, M.; Zhang, Q.; Wang, D. Novel 1D/2D KWO/Ti<sub>3</sub>C<sub>2</sub>T<sub>x</sub> Nanocomposite-Based Acetone Sensor for Diabetes Prevention and Monitoring. *Chemosensors* **2020**, *8*, No. 102.
- (14) Maleski, K.; Mochalin, V. N.; Gogotsi, Y. Dispersions of Two-Dimensional Titanium Carbide MXene in Organic Solvents. *Chem. Mater.* **2017**, *29*, 1632–1640.
- (15) Chae, Y.; Kim, S. J.; Cho, S.-Y.; Choi, J.; Maleski, K.; Lee, B.-J.; Jung, H.-T.; Gogotsi, Y.; Lee, Y.; Ahn, C. W. An investigation into the factors governing the oxidation of two-dimensional Ti<sub>3</sub>C<sub>2</sub> MXene. *Nanoscale* **2019**, *11*, 8387–8393.
- (16) Wang, C.; Yin, L.; Zhang, L.; Xiang, D.; Gao, R. Metal Oxide Gas Sensors: Sensitivity and Influencing Factors. *Sensors* **2010**, *10*, 2088–2106.
- (17) Dey, A. Semiconductor metal oxide gas sensors: A review. *Mater. Sci. Eng. B* **2018**, 229, 206–217.
- (18) Tai, H.; Duan, Z.; He, Z.; Li, X.; Xu, J.; Liu, B.; Jiang, Y. Enhanced ammonia response of  $Ti_3C_2T_x$  nanosheets supported by  $TiO_2$  nanoparticles at room temperature. *Sens. Actuators, B* **2019**, 298, No. 126874.
- (19) Sardana, S.; Kaur, H.; Arora, B.; Aswal, D. K.; Mahajan, A. Self-Powered Monitoring of Ammonia Using an MXene/TiO<sub>2</sub>/Cellulose Nanofiber Heterojunction-Based Sensor Driven by an Electrospun Triboelectric Nanogenerator. ACS Sens. 2022, 7, 312–321.
- (20) Choi, J.; Kim, Y.-J.; Cho, S.-Y.; Park, K.; Kang, H.; Kim, S. J.; Jung, H.-T. In Situ Formation of Multiple Schottky Barriers in a  $\mathrm{Ti_3C_2}$  MXene Film and its Application in Highly Sensitive Gas Sensors. *Adv. Funct. Mater.* **2020**, *30*, No. 2003998.
- (21) Liu, S.; Wang, M.; Liu, G.; Wan, N.; Ge, C.; Hussain, S.; Meng, H.; Wang, M.; Qiao, G. Enhanced NO<sub>2</sub> gas-sensing performance of

- 2D  $Ti_3C_2/TiO_2$  nanocomposites by in-situ formation of Schottky barrier. *Appl. Surf. Sci.* **2021**, *567*, No. 150747.
- (22) Zhou, Y.; Wang, Y.; Wang, Y.; Yu, H.; Zhang, R.; Li, J.; Zang, Z.; Li, X. MXene Ti<sub>3</sub>C<sub>2</sub>T<sub>x</sub>-Derived Nitrogen-Functionalized Heterophase TiO<sub>2</sub> Homojunctions for Room-Temperature Trace Ammonia Gas Sensing. *ACS Appl. Mater. Interfaces* **2021**, *13*, 56485–56497.
- (23) Zhang, H.-F.; Xuan, J.-Y.; Zhang, Q.; Sun, M.-L.; Jia, F.-C.; Wang, X.-M.; Yin, G.-C.; Lu, S.-Y. Strategies and challenges for enhancing performance of MXene-based gas sensors: a review. *Rare Met.* **2022**, *41*, 3976–3999.
- (24) Sardana, S.; Mahajan, A. Edge-Site-Enriched  ${\rm Ti_3C_2T_x}$  MXene/ ${\rm MoS_2}$  Nanosheet Heterostructures for Self-Powered Breath and Environmental Monitoring. *ACS Appl. Nano Mater.* **2023**, *6*, 469–481.
- (25) Gasso, S.; Mahajan, A. Development of Highly Sensitive and Humidity Independent Room Temeprature NO<sub>2</sub> Gas Sensor Using Two Dimensional Ti<sub>3</sub>C<sub>2</sub>T<sub>x</sub> Nanosheets and One Dimensional WO<sub>3</sub> Nanorods Nanocomposite. ACS Sens. 2022, 7, 2454–2464.
- (26) Wen, J.; Song, Z.; Ding, J.; Wang, F.; Li, H.; Xu, J.; Zhang, C. MXene-derived TiO<sub>2</sub> nanosheets decorated with Ag nanoparticles for highly sensitive detection of ammonia at room temperature. *J. Mater. Sci. Technol.* **2022**, *114*, 233–239.
- (27) Song, Y.; Xu, Y.; Guo, Q.; Hua, Z.; Yin, F.; Yuan, W. MXene-Derived TiO<sub>2</sub> Nanoparticles Intercalating between RGO Nanosheets: An Assembly for Highly Sensitive Gas Detection. *ACS Appl. Mater. Interfaces* **2021**, *13*, 39772–39780.
- (28) Lipatov, A.; Alhabeb, M.; Lukatskaya, M. R.; Boson, A.; Gogotsi, Y.; Sinitskii, A. Effect of Synthesis on Quality, Electronic Properties and Environmental Stability of Individual Monolayer Ti<sub>3</sub>C<sub>2</sub> MXene Flakes. *Adv. Electron. Mater.* **2016**, *2*, No. 1600255.
- (29) Lipatov, A.; Loes, M. J.; Lu, H.; Dai, J.; Patoka, P.; Vorobeva, N. S.; Muratov, D. S.; Ulrich, G.; Kästner, B.; Hoehl, A.; Ulm, G.; Zeng, X. C.; Rühl, E.; Gruverman, A.; Dowben, P. A.; Sinitskii, A. Quasi-1D TiS<sub>3</sub> Nanoribbons: Mechanical Exfoliation and Thickness-Dependent Raman Spectroscopy. *ACS Nano* 2018, *12*, 12713–12720.
- (30) Island, J. O.; Buscema, M.; Barawi, M.; Clamagirand, J. M.; Ares, J. R.; Sánchez, C.; Ferrer, I. J.; Steele, G. A.; van der Zant, H. S. J.; Castellanos-Gomez, A. Ultrahigh Photoresponse of Few-Layer TiS<sub>3</sub> Nanoribbon Transistors. *Adv. Opt. Mater.* **2014**, *2*, 641–645.
- (31) Lipatov, A.; Wilson, P. M.; Shekhirev, M.; Teeter, J. D.; Netusil, R.; Sinitskii, A. Few-layered titanium trisulfide (TiS<sub>3</sub>) field-effect transistors. *Nanoscale* **2015**, *7*, 12291–12296.
- (32) Finkman, E.; Fisher, B. Electrical transport measurements in TiS<sub>3</sub>. Solid State Commun. **1984**, 50, 25–28.
- (33) Yi, H.; Komesu, T.; Gilbert, S.; Hao, G.; Yost, A. J.; Lipatov, A.; Sinitskii, A.; Avila, J.; Chen, C.; Asensio, M. C.; Dowben, P. A. The band structure of the quasi-one-dimensional layered semiconductor TiS<sub>3</sub>(001). *Appl. Phys. Lett.* **2018**, *112*, No. 052102.
- (34) Dai, J.; Zeng, X. C. Titanium Trisulfide Monolayer: Theoretical Prediction of a New Direct-Gap Semiconductor with High and Anisotropic Carrier Mobility. *Angew. Chem., Int. Ed.* **2015**, *54*, 7572–7576.
- (35) Cui, Q.; Lipatov, A.; Wilt, J. S.; Bellus, M. Z.; Zeng, X. C.; Wu, J.; Sinitskii, A.; Zhao, H. Time-Resolved Measurements of Photocarrier Dynamics in TiS<sub>3</sub> Nanoribbons. *ACS Appl. Mater. Interfaces* **2016**, *8*, 18334–18338.
- (36) Island, J. O.; Barawi, M.; Biele, R.; Almazán, A.; Clamagirand, J. M.; Ares, J. R.; Sánchez, C.; van der Zant, H. S. J.; Álvarez, J. V.; D'Agosta, R.; Ferrer, I. J.; Castellanos-Gomez, A. TiS<sub>3</sub> Transistors with Tailored Morphology and Electrical Properties. *Adv. Mater.* **2015**, *27*, 2595–2601.
- (37) Papadopoulos, N.; Frisenda, R.; Biele, R.; Flores, E.; Ares, J. R.; Sánchez, C.; Van Der Zant, H. S. J.; Ferrer, I. J.; D'Agosta, R.; Castellanos-Gomez, A. Large birefringence and linear dichroism in TiS<sub>3</sub> nanosheets. *Nanoscale* **2018**, *10*, 12424–12429.
- (38) Liu, S.; Xiao, W.; Zhong, M.; Pan, L.; Wang, X.; Deng, H.-X.; Liu, J.; Li, J.; Wei, Z. Highly polarization sensitive photodetectors based on quasi-1D titanium trisulfide (TiS<sub>3</sub>). *Nanotechnology* **2018**, 29, No. 184002.

- (39) Gilbert, S. J.; Yi, H.; Chen, J.-S.; Yost, A. J.; Dhingra, A.; Abourahma, J.; Lipatov, A.; Avila, J.; Komesu, T.; Sinitskii, A.; Asensio, M. C.; Dowben, P. A. Effect of Band Symmetry on Photocurrent Production in Quasi-One-Dimensional Transition-Metal Trichalcogenides. ACS Appl. Mater. Interfaces 2020, 12, 40525–40531.
- (40) Randle, M. D.; Lipatov, A.; Mansaray, I.; Han, J. E.; Sinitskii, A.; Bird, J. P. Collective states and charge density waves in the group IV transition metal trichalcogenides. *Appl. Phys. Lett.* **2021**, *118*, No. 210502.
- (41) Gorlova, I. G.; Pokrovskii, V. Y. Collective conduction mechanism in a quasi-one-dimensional TiS<sub>3</sub> compound. *JETP Lett.* **2009**, *90*, 295–298.
- (42) Randle, M.; Lipatov, A.; Kumar, A.; Kwan, C.-P.; Nathawat, J.; Barut, B.; Yin, S.; He, K.; Arabchigavkani, N.; Dixit, R.; Komesu, T.; Avila, J.; Asensio, M. C.; Dowben, P. A.; Sinitskii, A.; Singisetti, U.; Bird, J. P. Gate-Controlled Metal–Insulator Transition in TiS<sub>3</sub> Nanowire Field-Effect Transistors. *ACS Nano* **2019**, *13*, 803–811.
- (43) Gorlova, I. G.; Pokrovskii, V. Y.; Gavrilkin, S. Y.; Tsvetkov, A. Y. Change in the Sign of the Magnetoresistance and the Two-Dimensional Conductivity of the Layered Quasi-One-Dimensional Semiconductor TiS<sub>3</sub>. *JETP Lett.* **2018**, *107*, 175–181.
- (44) Papadopoulos, N.; Flores, E.; Watanabe, K.; Taniguchi, T.; Ares, J. R.; Sanchez, C.; Ferrer, I. J.; Castellanos-Gomez, A.; Steele, G. A.; van der Zant, H. S. J. Multi-terminal electronic transport in boron nitride encapsulated TiS<sub>3</sub> nanosheets. 2D Mater. **2020**, 7, No. 015009.
- (45) Frisenda, R.; Giovanelli, E.; Mishra, P.; Gant, P.; Flores, E.; Sanchez, C.; Ares, J. R.; de Lara, D. P.; Ferrer, I. J.; Perez, E. M.; Castellanos-Gomez, A. Dielectrophoretic assembly of liquid-phase-exfoliated TiS<sub>3</sub> nanoribbons for photodetecting applications. *Chem. Commun.* **2017**, 53, 6164–6167.
- (46) Baraghani, S.; Abourahma, J.; Barani, Z.; Mohammadzadeh, A.; Sudhindra, S.; Lipatov, A.; Sinitskii, A.; Kargar, F.; Balandin, A. A. Printed Electronic Devices with Inks of TiS<sub>3</sub> Quasi-One-Dimensional van der Waals Material. *ACS Appl. Mater. Interfaces* **2021**, *13*, 47033–47042.
- (47) Sysoev, V. V.; Lashkov, A. V.; Lipatov, A.; Plugin, I. A.; Bruns, M.; Fuchs, D.; Varezhnikov, A. S.; Adib, M.; Sommer, M.; Sinitskii, A. UV-Light-Tunable p-/n-Type Chemiresistive Gas Sensors Based on Quasi-1D TiS<sub>3</sub> Nanoribbons: Detection of Isopropanol at ppm Concentrations. *Sensors* **2022**, 22, No. 9815.
- (48) Vorobeva, N. S.; Bagheri, S.; Torres, A.; Sinitskii, A. Negative photoresponse in Ti<sub>3</sub>C<sub>2</sub>T<sub>x</sub> MXene monolayers. *Nanophotonics* **2022**, *11*, 3953–3960.
- (49) Bagheri, S.; Chilcott, R.; Luo, S.; Sinitskii, A. Bifunctional Amine- and Thiol-Modified  ${\rm Ti_3C_2T_x}$  MXene for Trace Detection of Heavy Metals. *Langmuir* **2022**, 38, 12924–12934.
- (50) Bagheri, S.; Abourahma, J.; Lu, H.; Vorobeva, N. S.; Luo, S.; Gruverman, A.; Sinitskii, A. High-yield fabrication of electromechanical devices based on suspended Ti<sub>3</sub>C<sub>2</sub>T<sub>x</sub> MXene monolayers. *Nanoscale* **2023**, *15*, 1248–1259.
- (51) Gilbert, S. J.; Lipatov, A.; Yost, A. J.; Loes, M. J.; Sinitskii, A.; Dowben, P. A. The electronic properties of Au and Pt metal contacts on quasi-one-dimensional layered TiS<sub>3</sub>(001). *Appl. Phys. Lett.* **2019**, *114*, No. 101604.
- (52) Lipatov, A.; Varezhnikov, A.; Wilson, P.; Sysoev, V.; Kolmakov, A.; Sinitskii, A. Highly selective gas sensor arrays based on thermally reduced graphene oxide. *Nanoscale* **2013**, *5*, 5426–5434.
- (53) Lipatov, A.; Guinel, M. J.-F.; Muratov, D. S.; Vanyushin, V. O.; Wilson, P. M.; Kolmakov, A.; Sinitskii, A. Low-temperature thermal reduction of graphene oxide: In situ correlative structural, thermal desorption, and electrical transport measurements. *Appl. Phys. Lett.* **2018**, *112*, No. 053103.
- (54) Pour, M. M.; Lashkov, A.; Radocea, A.; Liu, X.; Sun, T.; Lipatov, A.; Korlacki, R. A.; Shekhirev, M.; Aluru, N. R.; Lyding, J. W.; Sysoev, V.; Sinitskii, A. Laterally extended atomically precise graphene nanoribbons with improved electrical conductivity for efficient gas sensing. *Nat. Commun.* **2017**, *8*, No. 820.

- (55) Shekhirev, M.; Lipatov, A.; Torres, A.; Vorobeva, N. S.; Harkleroad, A.; Lashkov, A.; Sysoev, V.; Sinitskii, A. Highly Selective Gas Sensors Based on Graphene Nanoribbons Grown by Chemical Vapor Deposition. ACS Appl. Mater. Interfaces 2020, 12, 7392–7402.
- (56) Ahn, S.; Han, T.-H.; Maleski, K.; Song, J.; Kim, Y.-H.; Park, M.-H.; Zhou, H.; Yoo, S.; Gogotsi, Y.; Lee, T.-W. A 2D Titanium Carbide MXene Flexible Electrode for High-Efficiency Light-Emitting Diodes. *Adv. Mater.* **2020**, *32*, No. 2000919.
- (57) Lipatov, A.; Goad, A.; Loes, M. J.; Vorobeva, N. S.; Abourahma, J.; Gogotsi, Y.; Sinitskii, A. High electrical conductivity and breakdown current density of individual monolayer  ${\rm Ti}_3{\rm C}_2{\rm T}_x$  MXene flakes. *Matter* **2021**, *4*, 1413–1427.
- (58) Yamazoe, N.; Shimanoe, K.Fundamentals of Semiconductor Gas Sensors. In *Semiconductor Gas Sensors*; Woodhead Publishing, 2020; pp 3–38.
- (59) Ghasemi, F.; Frisenda, R.; Flores, E.; Papadopoulos, N.; Biele, R.; de Lara, D. P.; van der Zant, H. S. J.; Watanabe, K.; Taniguchi, T.; D'Agosta, R.; Ares, J. R.; Sanchez, C.; Ferrer, I. J.; Castellanos-Gomez, A. Tunable Photodetectors via In Situ Thermal Conversion of TiS<sub>3</sub> to TiO<sub>2</sub>. Nanomaterials **2020**, *10*, No. 711.
- (60) Natu, V.; Benchakar, M.; Canaff, C.; Habrioux, A.; Célérier, S.; Barsoum, M. W. A critical analysis of the X-ray photoelectron spectra of Ti<sub>3</sub>C<sub>2</sub>T<sub>2</sub> MXenes. *Matter* **2021**, *4*, 1224–1251.
- (61) Benchakar, M.; Loupias, L.; Garnero, C.; Bilyk, T.; Morais, C.; Canaff, C.; Guignard, N.; Morisset, S.; Pazniak, H.; Hurand, S.; Chartier, P.; Pacaud, J.; Mauchamp, V.; Barsoum, M. W.; Habrioux, A.; Célérier, S. One MAX phase, different MXenes: A guideline to understand the crucial role of etching conditions on Ti<sub>3</sub>C<sub>2</sub>T<sub>x</sub> surface chemistry. *Appl. Surf. Sci.* **2020**, *530*, No. 147209.
- (62) Krishnan, P.; Liu, M.; Itty, P. A.; Liu, Z.; Rheinheimer, V.; Zhang, M.-H.; Monteiro, P. J. M.; Yu, L. E. Characterization of photocatalytic TiO<sub>2</sub> powder under varied environments using near ambient pressure X-ray photoelectron spectroscopy. *Sci. Rep.* **2017**, *7*, No. 43298.